3D Periodic Orbiting of a Photothermal Bubble

Man Hu[1], Feng Wang[2],[*] Yuqi Li,[1] Li Chen,[1] Wenna Wu,[1] Peng Huo,[1] and Daosheng Deng[1],[†]

[1]*Department of Aeronautics and Astronautics, Fudan University, Shanghai 200433, China*
[2]*Center for Combustion Energy, Department of Energy and Power Engineering, Tsinghua University, Beijing 100084, China*

The spontaneous periodic oscillations of underwater bubbles are typically confined to a 1D direction or within a 2D plane, whereas realizing 3D autonomous motion of bubbles remains challenging. In this Letter, we present experimental observations of a 3D-periodic orbiting bubble, produced by directing a stationary near-infrared laser at hexane, thereby extending the spectrum of multimode motions beyond the 1D and 2D paradigms. Through numerical simulation by carefully investigating both the thermodynamic and hydrodynamic parameters of several liquids, this 3D-orbiting mode is attributed to the subtle interplay between the interfacial flow due to the thermal Marangoni effect and the bulk flow from the thermal buoyancy effect. Moreover, by developing a unified physical model to elucidate the effect of liquid properties on the motion modes, a phase diagram is constructed through a single dimensionless number ($\Sigma = ReSc/Ma$), providing a theoretical guidance to tailor the periodic oscillation modes. These findings not only reveal the underlying intriguing physicochemical hydrodynamics, but also possibly shed light on the bubble-mediated technologies.

Introduction—The motion of bubbles in liquids occurs frequently in daily phenomena and industrial applications [1–3], and this two-phase flow generally leads to fascinating dynamics [4,5]. For example, an air bubble rising in water performs intriguing trajectories, ranging from a straight path to a periodic zigzag or spiral motion [6,7]; the addition of bubbles offers the opportunity to modify the key aspects of the turbulent flows [8,9], and local gas supersaturation or the difference in the gas solubility of two immiscible liquids can promote bubble nucleation and formation [10,11].

Recently, studies of bubbles underwater mediated by external stimuli have been emerging due to the wide applications of bubbles in drug delivery, lithography, heat management, microassembly, and microfluidic chips [12–17]. Notably, photothermal bubbles, which are generated and driven by lasers interacting with liquids, are intriguing because of their advantages of simplicity and controllability [18]. Diverse bubble motions under complex flow fields exposed to laser irradiation have been identified. For example, the counterintuitive vertical bouncing of plasmonic bubbles occurs within a binary ethanol-water mixture due to the interplay between an upward thermal Marangoni flow and a downward solutal Marangoni flow [19]. The 3D trapping and manipulation of microbubbles in water are facilitated by both radial and longitudinal photothermal Marangoni forces [20,21].

Particularly, the 1D-bouncing and 2D-hovering modes of photothermal bubbles have been revealed by engineering a thermally conductive sapphire cover atop the liquid surface to efficiently release the heat to the surrounding ambient air [Figs. 1(a) and 1(b)] [22,23]. Qualitatively, a temperature inversion layer (δ_{inv}), as characterized by a temperature peak underneath the solid-liquid interface, develops. The thickness of this layer, on the order of hundreds of micrometers, is determined by the coupled heat transfer and the bulk buoyancy flow as the liquid is subjected to laser irradiation. As the bubble tends to minimize its surface energy in the high-temperature region [24], a 1D-bouncing mode of the bubble is consequently produced in water by a downward thermal Marangoni force (F_m^z) and an upward viscous drag force (F_v^z) [22].

Because the underlying physical mechanisms of this photothermal bubble motion in this system arise from the complex coupling between photothermal absorption, heat transfer, thermal Marangoni flow, and bulk hydrodynamical flow, they are strongly correlated with the thermodynamic and hydrodynamic properties of liquids [25]. Therefore, the motion of photothermal bubbles can likely be tailored in various liquids. Indeed, in ethanol, a 2D-hovering mode at the solid-liquid interface is induced, since the viscous drag force from the stagnation flow (F_v^x) becomes dominant, while the thermal Marangoni force (F_m^x) acts as a restorative force [Figs. 1(a) and 1(b)] [23].

In this Letter, we report an experimental observation of a periodic 3D-orbiting mode of the photothermal bubble within hexane. By carefully investigating the thermophysic and hydrodynamic parameters of the liquids, a unified

---

[*]Contact author: fengwang2023@tsinghua.edu.cn
[†]Contact author: dsdeng@fudan.edu.cn
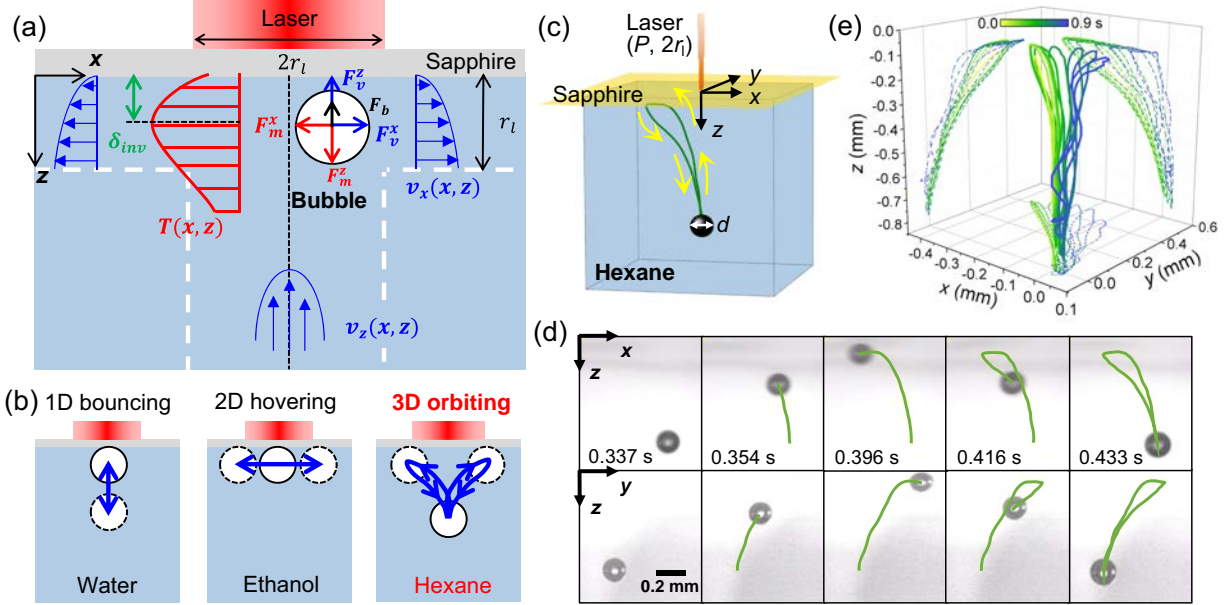
FIG. 1. Periodic 3D-orbiting mode of a photothermal bubble in hexane. (a) Sketch of the mechanism for the hydrodynamic flow and temperature distribution: the black dot line for the center of the incident laser, the vertical white dash line for the laser incident region, and the horizontal white dash line for the plane $z = r_l$. (b) Sketch of multimode motions. (c) Sketch of the 3D-orbiting trajectory of the bubble produced when a laser beam impacts hexane through a transparent cover glass. (d) High-speed images within one typical cycle from xz plane (the upper row) and yz plane (the lower row) at a laser power $P = 17$ W ($t = 0$ s for the instant when the bubble is visible). (e) Bubble trajectory during 0 to 0.9 s; the dashed lines correspond to the projections in the xy, xz, and yz planes.

physical model is developed to elucidate the underlying mechanism of the multimode motions. A phase diagram is constructed through a single dimensionless number ($\Sigma = ReSc/Ma$), providing theoretical guidance to tailor the periodic oscillation modes.

Observation of the 3D-orbiting bubble—A stationary 980-nm near-infrared laser (beam size $2r_l = 1$ mm) perpendicularly impacts hexane after passing through a 250-μm-thick sapphire glass, which is optically transparent at 185–5000 nm [Fig. 1(c)]. A photothermal bubble is formed within the liquid when the laser power exceeds the threshold value $P \approx 12$ W, corresponding to the averaged laser intensity $I \approx 1.5 \times 10^3$ W/cm^2, due to the volumetric absorption of photon energy (the absorption coefficient is about 3.65 m^{-1} at 980-nm wavelength for hexane [26]). The bubble motion is recorded by two high-speed cameras from two orthogonal side views (xz plane and yz plane), and the temperature evolution is recorded by a thermal camera (Supplemental Material [27], Note 1) [22,23].

Once generated within hexane, the bubble initially floats at the liquid-solid interface by touching the glass and then suddenly bounces back to be immersed in the liquid bulk [Fig. 1(d), and Video S1 in Supplemental Material). Differing from the 1D-bouncing mode along the z-axis direction in pure water [22] and the 2D-hovering mode within the xy-plane in ethanol [23], here the observed motion of the bubble in hexane is characterized by periodic 3D-orbiting oscillation, as demonstrated by the projected trajectories [Fig. 1(e)] and the decomposition of the

displacement along each axis for $d_{low} < d < d_{up}$ in the green shadow regime [Fig. 2(a)]. For the further increased bubble size ($d > d_{up}$), the buoyancy force can be dominant along the z direction; therefore, the bubble motion transitions from the 3D-orbiting mode to the 2D-hovering mode with the disappearance of oscillation along the z-axis direction.

Dynamics of 3D-orbiting mode—In the 3D-orbiting mode, the growth of the bubble diameter is dominated by the thermal diffusion, $d(t) \propto t^{1/2}$ (Supplemental Material, Note 2) [28]. The lower bound diameter of this mode in hexane in experiments is nearly a constant $d_{low} \approx 0.11$ mm [Fig. 2(b)]. With the increase of the bubble diameter, the buoyancy effect becomes more pronounced and the 3D-orbiting mode is suppressed. The upper bound diameter can be described by balancing a downward thermal Marangoni force [$F_m^z \sim (dT/dz)\delta_{inv}d \sim P^{3/4}d$] with an upward buoyancy force ($F_b \sim d^3$), $d_{up} \sim P^{3/8}$, consistent with the analysis for the 1D-bouncing mode in water [22].

For this 3D-orbiting mode, the probability density function of the periodic frequency (f) is obtained with a peak frequency $f_0 \sim 10$ Hz by applying Fourier analysis of the spatiotemporal evolution of bubble center position (x, y, z) within 0.7 s (Supplemental Material, Note 2). Furthermore, by presenting the motion frequency f_0 at different bubble diameters (d) and incident laser powers (P) [Fig. 2(c)], the lower bound frequency $f_0 \sim d^{1/2}$ corresponds to the buoyancy-dominant frequency in the 1D-bouncing mode [22], and the upper bound frequency $f_0 \sim d^{-1}$ is correlated
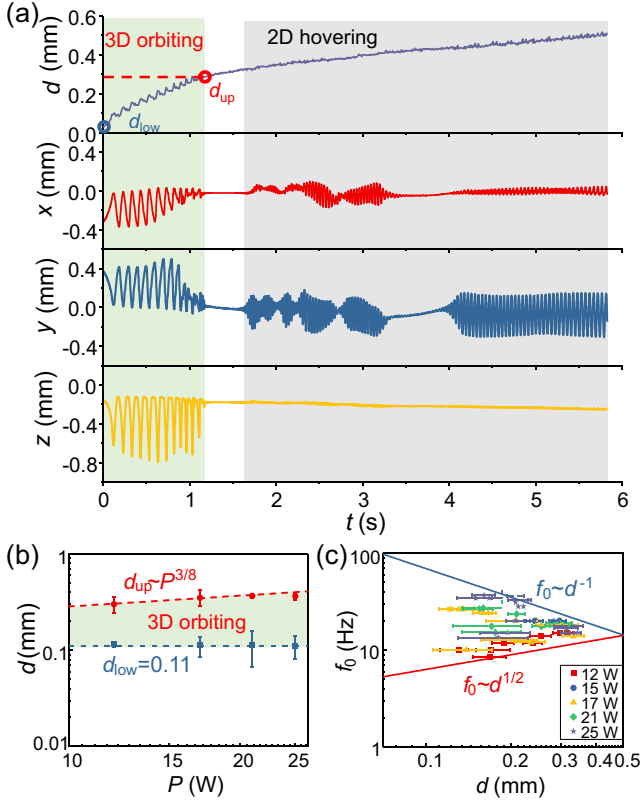
FIG. 2. Dynamics of the 3D-orbiting mode. (a) Time-dependent bubble diameter d, and center position (x, y, z), indicating the 3D-orbiting mode in the regime $d_{low} < d < d_{up}$ as highlighted by a green shadow, and the subsequent 2D-hovering mode later. (b) The lower (d_{low}) and upper bound (d_{up}) diameter dependent on the laser power (P). (c) f_0 dependent on the laser power (P) and bubble diameter (d).

with the thermal-Marangoni-dominant frequency in the 2D-hovering mode [23]. The observed frequency of the 3D-orbiting mode lies within these two scaling relations, implying the 3D-orbiting mode might be a synergistic coupling mode between the 1D-bouncing mode and the 2D-hovering mode.

Multimode motions in different liquids—As shown in the sketch [Figs. 1(a) and 1(b)], besides the 1D-bouncing mode [22] and the 2D-hovering mode [23], we have identified the 3D-orbiting mode in hexane (Video S2 in Supplemental Material), and a unified physical model is proposed to describe the preferable motion mode of bubbles. The volumetric heating effect of the incident laser generates an upward buoyancy flow [$v_z(x, z)$] within liquids, which sweeps across the liquid-solid (sapphire) interface, subsequently forming the viscous boundary layer [$v_x(x, z)$] and the thermal boundary layer. Additionally, the competition between the conductive cooling effect of the solid cover and the volumetric heating effect of the incident laser produces a pronounced temperature inversion layer [$T(x, z)$], which is characterized by a maximum temperature T_{max} at $z = \delta_{inv}$ [22] (Supplemental Material, Note 4).

To reveal the underlying temperature distribution and velocity field at a microscopic level within different liquids, we perform a numerical simulation for the coupled Navier-Stokes and heat transfer equations by carefully considering both thermodynamic and hydrodynamic properties [such as the absorption coefficient (α) at the laser wavelength, the thermal expansion coefficient (β), and viscosity (μ)] (Supplementary Table and Note 5) [22,23]. The typical snapshots within hexane are acquired at $P = 20$ W [Fig. 3(a)]. By changing the physical properties, we obtain the laser-induced temperature distribution and flow field at the different incident laser powers [Figs. 3(b)–3(h)]. The 1D-bouncing mode is determined by the thickness of the temperature inversion layer ($\delta_{inv} \sim Ra^{-1/4}$) [22,29], where the Rayleigh number $Ra = \beta \Delta T_z \rho g L^3 / \mu \kappa$, ΔT_z is the typical temperature difference along the z direction, $L = r_l$, ρ, κ for the typical length scale, the density, and thermal diffusivity of the liquid, respectively. The calculated δ_{inv}, $\delta_{inv}^{water} > \delta_{inv}^{ethanol} > \delta_{inv}^{hexane}$ [Fig. 3(b)], is consistent with experiments (Fig. S4 in Supplemental Material).

In order to highlight the effect of liquid properties on the multimode motions of bubbles (Supplementary Table), we will focus on the case of small bubble size ($d \ll d_{up}$), and thus the buoyancy force $F_b \sim d^3$ could be ignored. The laser radius (r_l) is taken as the characteristic length scale to assess the typical temperature difference ΔT_i and velocity v_i along the i-axis direction ($i = x, z$ direction), determining the thermal Marangoni force F_m^i and the viscous drag force F_v^i.

1D-bouncing mode—Because of the existence of the temperature inversion layer ($dT/dz > 0$), a downward thermal Marangoni force is exerted on the bubble [22], $F_m^z = \Delta \gamma_z \cdot d \sim (\partial \gamma / \partial T) \Delta T_z \cdot d$, where $\Delta T_z(x, z) = T(0, \delta_{inv}) - T(0,0)$ is the typical temperature difference along the z direction within the temperature inversion layer. Meanwhile, an upward viscous drag force is applied on the bubble by an upward buoyancy flow, $F_v^z = -6\pi\mu v_z d$ [30], where $v_z(x, z) = v_z(0, r_l) \sim Ra^{1/2}$ [22,29].

By comparing the upward viscous drag force and the downward thermal Marangoni force, a dimensionless number for 1D-bouncing criterion is obtained,

$$\xi_z = \frac{F_v^z}{F_m^z} \sim \frac{6\pi\mu v_z}{(\partial\gamma/\partial T)\Delta T_z}. \tag{1}$$

By incorporating simulation results of $\Delta T_z^{water} > \Delta T_z^{ethanol} > \Delta T_z^{hexane}$ [Fig. 3(c)] and $v_z^{hexane} > v_z^{ethanol} > v_z^{water}$ [Fig. 3(d)] into the above equation, the ratio ξ_z is obtained [Fig. 3(e)]. When the ratio ξ_z is large, the upward viscous drag force F_v^z is dominant, then the bubble is attached to the liquid-solid interface. Conversely, when the ratio ξ_z is small, the downward thermal Marangoni force F_m^z is dominant, and then the bubble is preferable to the 1D-bouncing mode. Since the pronounced bouncing motion is not observed in ethanol [Fig. 3(e)], the
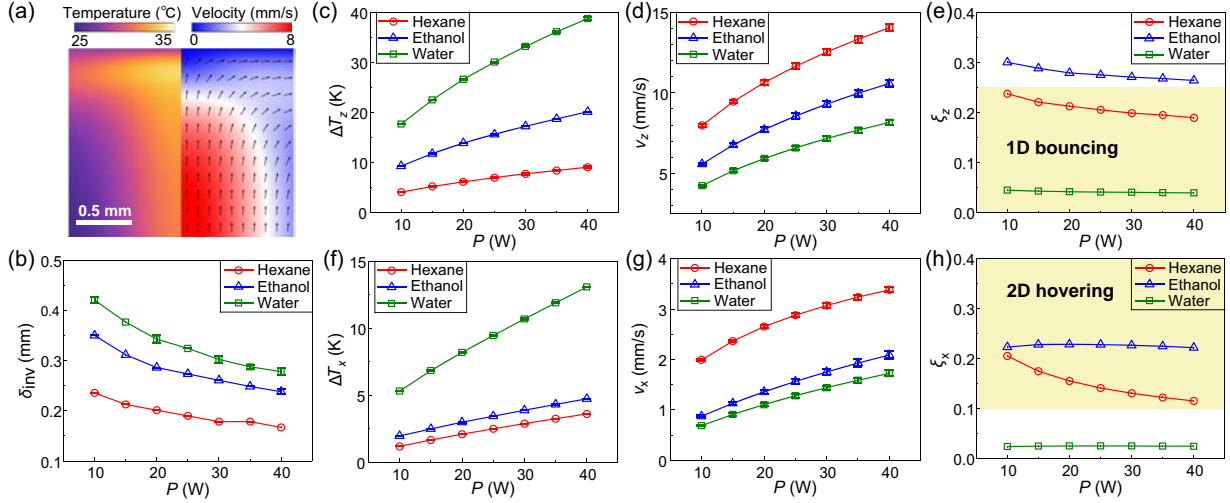
FIG. 3. Simulation of temperature distribution and hydrodynamic flow within different liquids. (a) Snapshot for the temperature distribution and flow field in hexane at $P = 20$ W. (b) Temperature inversion layer δ_{inv} in different liquids. (c)–(e) The 1D-bouncing mode: (c) temperature difference ΔT_z, (d) flow velocity v_z, and (e) force ratio ξ_z along the z direction, indicating the preferable 1D-bouncing mode in hexane and water. (f)–(h) The 2D-hovering mode: (f) temperature difference ΔT_x, (g) flow velocity v_x, and (h) force ratio ξ_x along the x direction, indicating the preferable 2D-hovering mode in hexane and ethanol. The error bars for the standard deviation within $t = 10$–20 s in simulations.

corresponding relation can be expected as $\xi_z^{\mathrm{ethanol}} > \xi_z^{\mathrm{crit}} > \xi_z^{\mathrm{hexane}} > \xi_z^{\mathrm{water}}$ ($\xi_z^{\mathrm{crit}} \approx 0.25$ here).

2D-hovering mode—Similarly, for the 2D-hovering mode at the solid-liquid interface, the existence of the horizontal temperature gradient results in a restoring thermal Marangoni force F_m^x to drive the bubble back to the center [23], $F_m^x = \Delta\gamma_x \cdot d \sim (\partial\gamma/\partial T)\Delta T_x \cdot d$, where the typical temperature difference along the x direction ΔT_x is defined as $\Delta T_x(x, z) = T(0, r_l) - T(r_l, r_l)$, where the origin of the x axis $(x = 0)$ is at the center of the incident laser. Meanwhile, due to the presence of the stagnation flow $v_x(x, z)$, the disturbing viscous drag force pushes the bubble away from the center, $F_v^x = -6\pi\mu v_x d$, where the typical velocity along the x direction v_x is defined as $v_x(x, z) = v_x(r_l, r_l)$.

By comparing the disturbing viscous drag force and the restoring thermal Marangoni force, a dimensionless number for 2D-hovering criterion is obtained,

$$\xi_x = \frac{F_v^x}{F_m^x} \sim \frac{6\pi\mu v_x}{(\partial\gamma/\partial T)\Delta T_x}. \qquad (2)$$

By incorporating simulation of ΔT_x [Fig. 3(f)] and velocity v_x [Fig. 3(g)] into Eq. (2), the ratio ξ_x is attained [Fig. 3(h)]. When the ratio ξ_x is large, the disturbing viscous drag force F_v^x is dominant, and then the bubble is preferable to the 2D-hovering mode. Conversely, when the ratio ξ_x is small, the restoring thermal Marangoni force F_m^x is dominant, and then it is preferable for the bubble to stay at the center. Since the horizontal oscillating motion is weak in water, the corresponding relation can be expected as $\xi_x^{\mathrm{ethanol}} > \xi_x^{\mathrm{hexane}} > \xi_x^{\mathrm{crit}} > \xi_x^{\mathrm{water}}$ ($\xi_x^{\mathrm{crit}} \approx 0.1$ in this work), as shown in Fig. 3(h).

Phase diagram—According to the aforementioned analysis, the multimode motions of the bubble within different liquids are determined by the force balance between the thermal Marangoni force ($F_m^i = \Delta\gamma_i d$) and the viscous drag force ($F_v^i = 6\pi\mu v_i d$) along each axis. Generally, the mode of bubble motion is determined by the ratio of these two competitive forces as below,
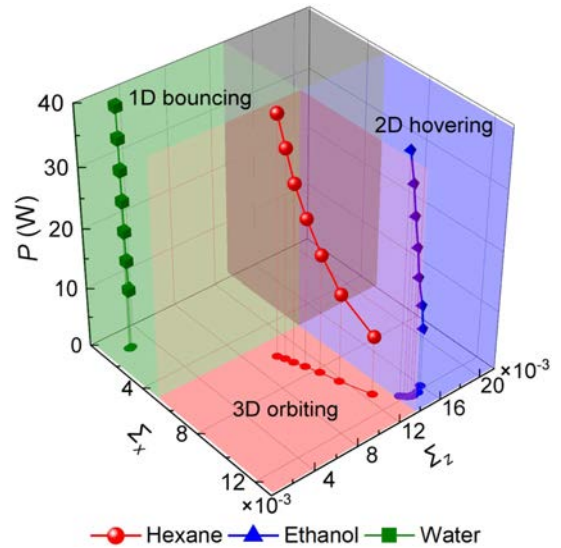
FIG. 4. Phase diagram of multimode motions for the photothermal bubble in three different liquids. The 1D-bouncing mode in water (the green shaded region), the 2D-hovering mode in ethanol (the blue shaded region), and the 3D-orbiting mode in hexane (the red shaded region).

$$\Sigma_i = \frac{Re_i Sc}{Ma_i}, \qquad (3)$$

where the Reynolds number $Re_i = \rho v_i d/\mu$ for the bulk flow estimates the viscous drag force F_v^i exerting on bubbles by the thermal buoyancy flow, the Marangoni number $Ma_i = \Delta\gamma_i d/\mu D_m$ for the interfacial flow indicates an estimate of the thermal Marangoni effect, while the Schmidt number $Sc = \mu/\rho D_m$ for liquid properties (kinematic viscosity and molecular diffusivity).

By this scaling analysis of these three dimensionless numbers [Eq. (3)], a phase diagram of bubble multimode motions in pure liquids is obtained, as shown in Fig. 4. Firstly, when Σ_z is small, the downward thermal Marangoni force F_m^z is dominant along the z direction, and the 1D-bouncing mode occurs, which is the case for water and hexane [Fig. 3(e)]. Secondly, when Σ_x is large, the disturbing viscous drag force F_v^x is dominant along the x direction, and the bubble tends to be in the 2D-hovering mode, which is the case for hexane and ethanol [Fig. 3(h)]. Within the overlapped regime of these two cases (smaller Σ_z and larger Σ_x), the bubble undergoes a strong coupling between the 1D-bouncing mode and the 2D-hovering mode, and results in the 3D-orbiting mode, consistent with the observation within hexane here.

Hence, by identifying a single dimensionless number Σ_i, which reflects the delicate competition and subtle interplay between the interfacial flow (Ma) and the bulk flow (Re), together with the liquid properties (Sc), the established phase diagram provides insight into the active tailoring of the oscillation modes among the 1D-bouncing, 2D-hovering, and 3D-orbiting modes. Moreover, by considering the scaling relation in natural convection $Re \sim Ra^{1/2}$ [29], the criteria for bubble motion [Eq. (3)] can be simplified into $\Sigma = Ra^{1/2}/Ma$, consistent with that for the bouncing droplet in a stratified liquid [31], highlighting a similar physical mechanism where the interfacial stress (Marangoni effect) competes with the bulk stress (viscous drag force).

[1] D. Lohse, Bubble puzzles: From fundamentals to applications, Phys. Rev. Fluids **3**, 110504 (2018).

[2] S. Park, L. Liu, Ç. Demirkır, O. van der Heijden, D. Lohse, D. Krug, and M. T. M. Koper, Solutal Marangoni effect determines bubble dynamics during electrocatalytic hydrogen evolution, Nat. Chem. **15**, 1532 (2023).

[3] D. Legendre and R. Zenit, Gas bubble dynamics, arXiv:2501.02988.

[4] J. Magnaudet and I. Eames, The motion of high-Reynolds-number bubbles in inhomogenous flow, Annu. Rev. Fluid Mech. **32**, 659 (2000).

[5] F. Risso, Agitation, mixing, and transfers induced by bubbles, Annu. Rev. Fluid Mech. **50**, 25 (2018).

[6] W. L. Shew and J. F. Pinton, Dynamical model of bubble path instability, Phys. Rev. Lett. **97**, 144508 (2006).

[7] M. A. Herrada and J. G. Eggers, Path instability of an air bubble rising in water, Proc. Natl. Acad. Sci. U.S.A. **120**, e2216830120 (2023).

[8] V. Mathai, E. Calzavarini, J. Brons, C. Sun, and D. Lohse, Microbubbles and microparticles are not faithful tracers of turbulent acceleration, Phys. Rev. Lett. **117**, 024501 (2016).

[9] V. Mathai, D. Lohse, and C. Sun, Bubbly and buoyant particle–laden turbulent flows, Annu. Rev. Condens. Matter Phys. **11**, 529 (2020).

[10] P. Pfeiffer, J. Eisener, H. Reese, M. Li, X. Ma, C. Sun, and C. D. Ohl, Thermally assisted heterogeneous cavitation through gas supersaturation, Phys. Rev. Lett. **128**, 194501 (2022).

[11] P. Pfeiffer, M. Shahrooz, M. Tortora, C. M. Casciola, R. Holman, R. Salomir, S. Meloni, and C.-D. Ohl, Heterogeneous cavitation from atomically smooth liquid–liquid interfaces, Nat. Phys. **18**, 1431 (2022).

[12] Y. Gao, M. Wu, Y. Lin, and J. Xu, Trapping and control of bubbles in various microfluidic applications, Lab Chip **20**, 4512 (2020).

[13] K. J. Chen, H.-F. Liang, H.-L. Chen, Y. Wang, P.-Y. Cheng, H.-L. Liu, Y. Xia, and H.-W. Sung, A thermoresponsive bubble-generating liposomal system for triggering localized extracellular drug delivery, ACS Nano **7**, 438 (2013).

[14] L. Lin, X. Peng, Z. Mao, W. Li, M. N. Yogeesh, B. B. Rajeeva, E. P. Perillo, A. K. Dunn, D. Akinwande, and Y. Zheng, Bubble-pen lithography, Nano Lett. **16**, 701 (2016).

[15] X. Liang *et al.*, Manipulation of droplets and bubbles for thermal applications, Droplet **1**, 80 (2022).

[16] L. G. Dai, D. Lin, X. Wang, N. Jiao, and L. Liu, Integrated assembly and flexible movement of microparts using multifunctional bubble microrobots, ACS Appl. Mater. Interfaces **12**, 57587 (2020).

[17] Y. Y. Li, X. Liu, Q. Huang, A. T. Ohta, and T. Arai, Bubbles in microfluidics: An all-purpose tool for micromanipulation, Lab Chip **21**, 1016 (2021).

[18] F. L. Wang, Z. Wang, L. Dong, H. Liu, L. Yang, and Y. Wang, Plasmonic bubbles: From fundamentals to applications, Adv. Funct. Mater. **34**, 2403606 (2024).

[19] B. L. Zeng, K. L. Chong, Y. Wang, C. Diddens, X. Li, M. Detert, H. J. W. Zandvliet, and D. Lohse, Periodic bouncing of a plasmonic bubble in a binary liquid by competing solutal and thermal Marangoni forces, Proc. Natl. Acad. Sci. U.S.A. **118**, e2103215118 (2021).

[20] J. A. Sarabia-Alonso, J. G. Ortega-Mendoza, S. Mansurova, F. M. Muñoz-Pérez, and R. Ramos-García, 3D trapping of microbubbles by the Marangoni force, Opt. Lett. **46**, 5786 (2021).

[21] J. A. Sarabia-Alonso, J. M. Pérez-Corte, J. G. Ortega-Mendoza, K. Ortega-Sánchez, A. Becerra-Hernández, A. Gúzman-Barraza, and R. Ramos-García, Self-oscillation of 3D trapped bubbles, Opt. Laser Technol. **172**, 110509 (2024).

[22] M. Hu, F. Wang, L. Chen, P. Huo, Y. Li, X. Gu, K. L. Chong, and D. Deng, Near-infrared-laser-navigated dancing bubble within water via a thermally conductive interface, Nat. Commun. **13**, 5749 (2022).

[23] M. Hu, Y. Li, L. Chen, W. Wu, P. Huo, X. Gu, F. Wang, and D. Deng, A hovering bubble with a spontaneous horizontal oscillation, Proc. Natl. Acad. Sci. U.S.A. **121**, e2413880121 (2024).

[24] N. O. Young, J. S. Goldstein, and M. J. Block, The motion of bubbles in a vertical temperature gradient, J. Fluid Mech. **6**, 350 (1959).

[25] D. Lohse and X. H. Zhang, Physicochemical hydrodynamics of droplets out of equilibrium, Nat. Rev. Phys. **2**, 426 (2020).

[26] A. J. Rest, R. Warren, and S. C. Murray, Near-infrared study of the light liquid alkanes, Appl. Spectrosc. **50**, 517 (1996).

[27] See Supplemental Material at http://link.aps.org/supplemental/10.1103/PhysRevLett.134.104004 for two supplementary movies, more details of experimental setup, experimental results, numerical simulations and liquid properties.

[28] M. S. Plesset and S. A. Zwick, A nonsteady heat diffusion problem with spherical symmetry, J. Appl. Phys. **23**, 95 (1952).

[29] S. Grossmann and D. Lohse, Scaling in thermal convection: A unifying theory, J. Fluid Mech. **407**, 27 (2000).

[30] R. Toegel, S. Luther, and D. Lohse, Viscosity destabilizes sonoluminescing bubbles, Phys. Rev. Lett. **96**, 114301 (2006).

[31] Y. Li, C. Diddens, A. Prosperetti, and D. Lohse, Marangoni instability of a drop in a stably stratified liquid, Phys. Rev. Lett. **126**, 124502 (2021).